



CrossMark  
click for updates

Cite this: *RSC Adv.*, 2015, 5, 70992

## Second harmonic generation from the novel polar polymorph $\alpha/\beta$ -BaTeMo<sub>2</sub>O<sub>9</sub> phases†‡

A. H. Reshak\*<sup>ab</sup>

The second harmonic generation (SHG) and the first hyperpolarizability ( $\beta_{ijk}$ ) of  $\beta$ -BaTeMo<sub>2</sub>O<sub>9</sub> and  $\alpha$ -BaTeMo<sub>2</sub>O<sub>9</sub> phases have been calculated. Due to structure arrangement and hence the orientation of the dipole moments,  $\beta$ -phase exhibit larger SHG than that of  $\alpha$ -phase although it produces high local SHG. The linear optical properties reveals that  $\alpha$ -phase show larger anisotropy between the optical components along the polarization directions [100], [101] and [001] than that of  $\beta$ -phase. The anisotropy in the linear optical susceptibilities favors an enhanced phase matching conditions necessary for observation of SHG and optical parametric oscillation (OPO). It has been found that these materials exhibit positive uniaxial anisotropy and positive birefringence. We found that  $\alpha$ -phase show higher uniaxial anisotropy and birefringence values than those of  $\beta$ -phase. The calculated SHG reveals that  $\chi_{222}^{(2)}(\omega)$  is the dominant tensor compound for  $\beta$ -phase with  $d_{22}$  of about 20.46 pm V<sup>-1</sup> which is higher than the experimental value of the well known KTiOPO<sub>4</sub> (KTP) single crystals. While  $\chi_{322}^{(2)}(\omega)$  is the dominant tensor compound of  $\alpha$ -phase with  $d_{32}$  of about 0.11 pm V<sup>-1</sup>. In addition, we have calculated the microscopic first hyperpolarizability,  $\beta_{ijk}$ , the vector components along the dipole moment direction for the dominant components of  $\beta$ -BaTeMo<sub>2</sub>O<sub>9</sub> and  $\alpha$ -BaTeMo<sub>2</sub>O<sub>9</sub> phases at static limit and at  $\lambda = 1064$  nm.

Received 24th June 2015  
Accepted 10th August 2015

DOI: 10.1039/c5ra12198a

www.rsc.org/advances

### 1. Introduction

Noncentrosymmetric polar inorganic oxide materials are promising candidates for second order nonlinear optical applications namely second harmonic generation (SHG).<sup>1–3</sup> In the recent years there is potential interest in finding novel materials which can produce visible, ultraviolet and infra-red laser radiation at wavelengths that are presently inaccessible *via* conventional sources for many industrial, medical, biological and entertainment applications.<sup>4–6</sup> Noncentrosymmetric polar inorganic oxides are technologically important for several applications, such as piezoelectricity, nonlinear optical properties, ferroelectricity and pyroelectricity.<sup>7–9</sup> Fuks-Janczarek *et al.*<sup>8</sup> have used *Z*-scan measurements to investigate  $\beta$ -BaTeMo<sub>2</sub>O<sub>9</sub> single crystal, it has been found that  $\beta$ -BaTeMo<sub>2</sub>O<sub>9</sub> possess promising third-order optical susceptibilities. Further, they have used the first principles calculations based on CASTEP code to investigate the electronic band structure of  $\beta$ -BaTeMo<sub>2</sub>O<sub>9</sub> single crystal. Calculations show that this crystal have a direct band gap of about 2.61 eV using the local density approximation (LDA) and 2.67 eV using the

generalized gradient approximation (GGA). Zhang *et al.*<sup>9</sup> have used the first principles calculations based on ABINIT code within GGA to investigate the ferroelectric and optical properties of  $\beta$ -BaTeMo<sub>2</sub>O<sub>9</sub> single crystal, it has been found that the investigated crystal have a direct band gap of about 2.78 eV. Therefore, several research groups investigated the structural properties and the other related properties. Several polar oxides single crystals were synthesized, the suitability of polar oxides containing cations susceptible to second order Jahn–Teller distortions for nonlinear optical and piezoelectric application was investigated.<sup>10–13</sup> A novel polar polymorph  $\alpha$ -BaTeMo<sub>2</sub>O<sub>9</sub> phase was discovered by Zhang's group,<sup>1</sup> during the growing of  $\beta$ -BaTeMo<sub>2</sub>O<sub>9</sub> single crystal at temperature below 570 °C the product was pure  $\beta$ -BaTeMo<sub>2</sub>O<sub>9</sub> while with increasing the temperature up to 570 °C they found a small amount of  $\alpha$ -BaTeMo<sub>2</sub>O<sub>9</sub> phase started to appears in the product. Increasing the temperature above 570 °C the product converted to be a pure  $\alpha$ -BaTeMo<sub>2</sub>O<sub>9</sub>.<sup>1</sup> It has been found that both  $\beta$ - and  $\alpha$ -phases of BaTeMo<sub>2</sub>O<sub>9</sub> are thermally stable and the newly discovered phase ( $\alpha$ -phases) contains 2D-(Te<sub>2</sub>Mo<sub>4</sub>O<sub>18</sub>)<sup>4-</sup> anionic layers interleaved with Ba<sup>2+</sup> cations.<sup>1</sup> The newly discovered phase motivated several researchers to investigate the unique properties of this phase.<sup>2,3,14</sup> Recently, Raman spectra using pulsed laser diode pumped Nd:YAG/Cr<sup>4+</sup>:YAG was reported for  $\alpha$ -BaTeMo<sub>2</sub>O<sub>9</sub> phase,<sup>14</sup> they found that the high energy output pulse have potential application in medical treatment and laser ranging.<sup>14</sup> Using two continuous wave lasers 808 and 1064 nm as photoinducing sources Majchrowski *et al.*<sup>2</sup> have measured

<sup>a</sup>New Technologies-Research Centre, University of West Bohemia, Univerzitni 8, 306 14 Pilsen, Czech Republic. E-mail: maalidph@yahoo.co.uk

<sup>b</sup>Center of Excellence Geopolymer and Green Technology, School of Material Engineering, University Malaysia Perlis, 01007 Kangar, Perlis, Malaysia

† PACS no.: 71.15 Mb and 71.20 b.

‡ Electronic supplementary information (ESI) available. See DOI: 10.1039/c5ra12198a

the SHG at the wavelength 1064 nm under photoinducing treatment of monoclinic piezoelectric  $\beta$ -BaTeMo<sub>2</sub>O<sub>9</sub>. An *ab initio* plane-wave pseudopotential total energy package CASTEP within the generalized gradient approximation (PBE-GGA) was used to calculate the refractive index and the birefringence of  $\alpha$ -BaTeMo<sub>2</sub>O<sub>9</sub> in the spectral range of 0.4–5.0  $\mu\text{m}$ .<sup>3</sup>

From the above it is clear that there exists some experimental and theoretical work on  $\beta$ -BaTeMo<sub>2</sub>O<sub>9</sub> and  $\alpha$ -BaTeMo<sub>2</sub>O<sub>9</sub> phases<sup>1–3,7–14</sup> we feel that there is a dearth information on the second harmonic generation and the microscopic first hyperpolarizability. Most the measurements of the SHG for  $\beta$ -BaTeMo<sub>2</sub>O<sub>9</sub> and  $\alpha$ -BaTeMo<sub>2</sub>O<sub>9</sub> phases were performed on powders without details descriptions about the complex second-order nonlinear optical susceptibility tensors, moreover no information regarding the microscopic first hyperpolarizability terms which cumulatively yield a bulk observable second order susceptibility term,  $\chi_{ijk}^{(2)}(\omega)$ , which in turn is responsible for the high SHG response. Therefore, we thought it is worthwhile to perform comprehensive theoretical calculation based on the density functional theory within full potential method and the recently modified Becke–Johnson potential (mBJ) to investigate the linear and nonlinear optical properties  $\beta$ -BaTeMo<sub>2</sub>O<sub>9</sub> and  $\alpha$ -BaTeMo<sub>2</sub>O<sub>9</sub> phases and the influence of the phase transition from  $\beta \rightarrow \alpha$  on the linear and nonlinear optical properties. In the recent years due to the improvement of the computational technologies, it has been proven that the first-principles calculation is a strong and useful tool to predict the crystal structure and its properties related to the electron configuration of a material before its synthesis.<sup>15,16</sup>

## 2. Calculation methodology

To investigate the linear and nonlinear optical properties of the two phases, the X-ray diffraction data obtained by Zhang *et al.*<sup>1</sup> were used as input data for comprehensive theoretical calculation. The experimental geometrical structures were optimized using the all-electron full potential linear augmented plane wave plus local orbitals (FP-LAPW + lo) method as implemented in WIEN2k code<sup>17</sup> within generalized gradient approximation (PBE-GGA).<sup>18</sup> The resulting relaxed geometry was used to calculate the linear and nonlinear optical properties using the recently modified Becke–Johnson potential (mBJ).<sup>19</sup> The modified Becke–Johnson potential allows the calculation with accuracy similar to the very expensive GW calculations.<sup>19</sup> It is a local approximation to an atomic “exact-exchange” potential and a screening term. The spherical harmonic expansion was used inside the non-overlapping spheres of muffin-tin radius ( $R_{\text{MT}}$ ) and the plane wave basis set was chosen in the interstitial region (IR) of the unit cell. The  $R_{\text{MT}}$  for Ba, Mo, Te and O atoms were chosen in such a way that the spheres did not overlap,

these values are 2.44 (2.47) a.u. for Ba  $\beta$  ( $\alpha$ ), 1.79 (1.83) a.u. for Te  $\beta$  ( $\alpha$ ), 1.61 (1.62) for Mo  $\beta$  ( $\alpha$ ) and 1.46 for  $\beta$  ( $\alpha$ ) O. To achieve the total energy convergence, the basis functions in the IR were expanded up to  $R_{\text{MT}} \times K_{\text{max}} = 7.0$  and inside the atomic spheres for the wave function. The maximum value of  $l$  were taken as  $l_{\text{max}} = 10$ , while the charge density is Fourier expanded up to  $G_{\text{max}} = 12.0$  (a.u.)<sup>-1</sup>. A self-consistency is obtained using 300  $\vec{k}$  points in the irreducible Brillouin zone (IBZ). The self-consistent calculations are converged since the total energy of the system is stable within 0.00001 Ry. The linear optical properties were calculated within 1000  $\vec{k}$  points in the IBZ while the nonlinear optical properties are obtained within 2000  $\vec{k}$  points in the IBZ.

It has been reported that the  $\beta$ -phase of BaTeMo<sub>2</sub>O<sub>9</sub> crystallized in non-centro-symmetric monoclinic structure with space group  $P2_1$ , while  $\alpha$ -phase crystallizes in non-centro-symmetric orthorhombic  $Pca2_1$  space group.<sup>1,10</sup> The monoclinic and orthorhombic symmetry allows three non-zero components of the second-order optical dielectric tensor corresponding to the electric field  $\vec{E}$  being directed along  $a$ ,  $b$ , and  $c$ -crystallographic axes. We identify these with the  $x$ ,  $y$  and  $z$  Cartesian directions. The imaginary part of the three principal complex tensor components completely defines the linear optical susceptibilities. These are  $\varepsilon_2^{xx}(\omega)$ ,  $\varepsilon_2^{yy}(\omega)$  and  $\varepsilon_2^{zz}(\omega)$  which originates from inter-band transitions between valence and conduction bands. According to the dipolar selection rule only transitions changing the angular momentum quantum number  $l$  by unity are allowed. The imaginary parts can be calculated using the following expression:<sup>20</sup>

$$\varepsilon_2^{ij}(\omega) = \frac{8\pi^2 \hbar^2 e^2}{m^2 V} \sum_k \sum_{cv} (f_c - f_v) \frac{p_{cv}^i(k) p_{vc}^j(k)}{E_{vc}^2} \times \delta[E_c(k) - E_v(k) - \hbar\omega] \quad (1)$$

where  $m$ ,  $e$  and  $\hbar$  are the electron mass, charge and Planck's constant, respectively.  $f_c$  and  $f_v$  represent the Fermi distributions of the conduction and valence bands, respectively. The term  $p_{cv}^i(k)$  denotes the momentum matrix element transition from the energy level  $c$  of the conduction band to the level  $v$  of the valence band at certain  $k$ -point in the BZ and  $V$  is the unit cell volume.

The complex second-order nonlinear optical susceptibility tensor  $\chi_{ijk}^{(2)}(-2\omega; \omega; \omega)$  can be generally written as:<sup>21–24</sup>

$$\chi_{\text{inter}}^{ijk}(-2\omega; \omega, \omega) = \frac{e^3}{\hbar^2} \sum_{\text{nmI}} \int \frac{d\vec{k}}{4\pi^3} \frac{\vec{r}_{\text{nm}}^i \left\{ \vec{r}_{\text{ml}}^j \vec{r}_{\text{ln}}^k \right\}}{(\omega_{\text{ln}} - \omega_{\text{ml}})} \times \left\{ \frac{2f_{\text{nm}}}{(\omega_{\text{mn}} - 2\omega)} + \frac{f_{\text{ml}}}{(\omega_{\text{ml}} - \omega)} + \frac{f_{\text{ln}}}{(\omega_{\text{ln}} - \omega)} \right\} \quad (2)$$

$$\chi_{\text{intra}}^{ijk}(-2\omega; \omega, \omega) = \frac{e^3}{\hbar^2} \int \frac{d\vec{k}}{4\pi^3} \left[ \sum_{\text{nmI}} \omega_{\text{nm}} \vec{r}_{\text{nm}}^i \left\{ \vec{r}_{\text{ml}}^j \vec{r}_{\text{ln}}^k \right\} \left\{ \frac{f_{\text{nl}}}{\omega_{\text{ln}}^2 (\omega_{\text{ln}} - \omega)} - \frac{f_{\text{lm}}}{\omega_{\text{ml}}^2 (\omega_{\text{ml}} - \omega)} \right\} - 8i \sum_{\text{nm}} \frac{f_{\text{nm}} \vec{r}_{\text{nm}}^i \left\{ \Delta_{\text{mn}}^j \vec{r}_{\text{nm}}^k \right\}}{\omega_{\text{mn}}^2 (\omega_{\text{mn}} - 2\omega)} + 2 \sum_{\text{nmI}} \frac{f_{\text{nm}} \vec{r}_{\text{nm}}^i \left\{ \vec{r}_{\text{ml}}^j \vec{r}_{\text{ln}}^k \right\} (\omega_{\text{ml}} - \omega_{\text{ln}})}{\omega_{\text{mn}}^2 (\omega_{\text{mn}} - 2\omega)} \right] \quad (3)$$

$$\chi_{\text{mod}}^{ijk}(-2\omega; \omega, \omega) = \frac{e^3}{2\hbar^2} \int \frac{d\vec{k}}{4\pi^3} \left[ \sum_{\text{nm}l} \frac{f_{\text{nm}}}{\omega_{\text{nm}}^2(\omega_{\text{nm}} - \omega)} \left\{ \omega_{\text{nl}} \vec{r}_{\text{nm}}^i \left\{ \vec{r}_{\text{mn}}^j \vec{r}_{\text{nl}}^k \right\} - \omega_{\text{lm}} \vec{r}_{\text{nl}}^i \left\{ \vec{r}_{\text{lm}}^j \vec{r}_{\text{mn}}^k \right\} \right\} - i \sum_{\text{nm}} \frac{f_{\text{nm}} \vec{r}_{\text{nm}}^i \left\{ \vec{r}_{\text{nm}}^j \Delta_{\text{mn}}^k \right\}}{\omega_{\text{nm}}^2(\omega_{\text{nm}} - \omega)} \right] \quad (4)$$

From these formulae we can notice that there are three major contributions to  $\chi_{ijk}^{(2)}(-2\omega; \omega, \omega)$ : the inter-band transitions  $\chi_{\text{inter}}^{ijk}(-2\omega; \omega, \omega)$ , the intra-band transitions  $\chi_{\text{intra}}^{ijk}(-2\omega; \omega, \omega)$  and the modulation of inter-band terms by intra-band terms  $\chi_{\text{mod}}^{ijk}(-2\omega; \omega, \omega)$ , where  $n \neq m \neq l$ . Here  $n$  denotes the valence states,  $m$  the conduction states and  $l$  denotes all states ( $l \neq m, n$ ). There are two kinds of transitions that can take place, one of them  $vcc'$ , involves one valence band ( $v$ ) and two conduction bands ( $c$  and  $c'$ ), and the second transition  $vv'c$ , involves two valence bands ( $v$  and  $v'$ ) and one conduction band ( $c$ ). The symbols are defined as  $\Delta_{\text{nm}}^i(\vec{k}) = \vartheta_{\text{nn}}^i(\vec{k}) - \vartheta_{\text{mm}}^i(\vec{k})$  with  $\vartheta_{\text{nm}}^i$  being the  $i$  component of the electron velocity given as  $\vartheta_{\text{nm}}^i(\vec{k}) = i\omega_{\text{nm}}(\vec{k})r_{\text{nm}}^i(\vec{k})$  and  $\{r_{\text{nm}}^i(\vec{k})r_{\text{ml}}^j(\vec{k})\} = \frac{1}{2}(r_{\text{nm}}^i(\vec{k})r_{\text{ml}}^j(\vec{k}) + r_{\text{nm}}^j(\vec{k})r_{\text{ml}}^i(\vec{k}))$ . The position matrix elements between band states  $n$  and  $m$ ,  $r_{\text{nm}}^i(\vec{k})$ , are calculated from the momentum matrix element  $P_{\text{nm}}^i$  using the relation:<sup>25</sup>  $r_{\text{nm}}^i(\vec{k}) = \frac{P_{\text{nm}}^i(\vec{k})}{im\omega_{\text{nm}}(\vec{k})}$ , with the energy difference between the states  $n$  and  $m$  given by  $\hbar\omega_{\text{nm}} = \hbar(\omega_n - \omega_m)$ .  $f_{\text{nm}} = f_n - f_m$  is the difference of the Fermi distribution functions.  $i, j$  and  $k$  correspond to Cartesian indices. It has been demonstrated that only the one-electron virtual transitions (transitions between one valence band state and two conduction band states,  $vcc'$ ) give a significant contribution to the second-order tensor.<sup>26</sup> We ignore the virtual-hole contribution (transitions between two valence band states and one conduction band state,  $vv'c$ ) because it was found to be negative and more than an order of magnitude smaller than the virtual-electron contribution for this compound. For simplicity we denote  $\chi_{ijk}^{(2)}(-2\omega; \omega, \omega)$  by  $\chi_{ijk}^{(2)}(\omega)$ . The subscripts  $i, j$ , and  $k$  are Cartesian indices.

It is clear that from the formulae (1)–(4) that the energy gap's value comes in the denominator of these formulae thus, the linear and nonlinear optical properties are very sensitive to the energy gap's value. Therefore, to obtain an accurate results it is necessary mBJ or similar approach.

### 3. Crystal structure of $\beta$ -BaTeMo<sub>2</sub>O<sub>9</sub> and $\alpha$ -BaTeMo<sub>2</sub>O<sub>9</sub>

The crystal structure of  $\beta$ -BaTeMo<sub>2</sub>O<sub>9</sub> and  $\alpha$ -BaTeMo<sub>2</sub>O<sub>9</sub> are shown in Fig. 1.  $\beta$ -BaTeMo<sub>2</sub>O<sub>9</sub> and  $\alpha$ -BaTeMo<sub>2</sub>O<sub>9</sub> are 2D layered structures. In the unit cell of  $\alpha$ -phase the length of two axes are almost double of that in  $\beta$ -phase.  $\beta$ -phase consist of two symmetry independent MoO<sub>6</sub> octahedra and one TeO<sub>4</sub> polyhedra which interconnect to form the 2D anionic layer, while  $\alpha$ -phase contains TeO<sub>3</sub>, TeO<sub>4</sub> polyhedra and MoO<sub>6</sub> octahedra, the MoO<sub>6</sub> combine with three nearest neighbor MoO<sub>6</sub> through the corners to form 1D-zigzag chain of the tetramer Mo<sub>4</sub>O<sub>20</sub>. The resulting Mo<sub>4</sub>O<sub>20</sub> linked to TeO<sub>3</sub> and TeO<sub>4</sub> to form the 2D anionic layer with Ba<sup>2+</sup> cations located between the layers.

In  $\beta$ -BaTeMo<sub>2</sub>O<sub>9</sub> phase the Te(1)O<sub>4</sub> polyhedra is formed between Te(1) with O(1), O(2), O(3) and O(4), and the two Mo(1)O<sub>6</sub> octahedra is formed between Mo(1) and O(1), O(3), O(4), O(5), O(6), O(7), the second Mo(2)O<sub>6</sub> octahedra is formed between Mo(2) and O(1), O(2), O(3), O(7), O(8), O(9). The asymmetric unit of  $\beta$ -BaTeMo<sub>2</sub>O<sub>9</sub> phase has a BaTeMo<sub>2</sub>O<sub>9</sub> formula as shown in Fig. 1(a). In  $\alpha$ -BaTeMo<sub>2</sub>O<sub>9</sub> the Te(1)O<sub>4</sub> polyhedra is formed between Te(1) with O(2), O(9), O(10) and O(11), the Te(2)O<sub>3</sub> polyhedra is formed between Te(2) with O(2), O(7) and O(18), the four Mo(1)O<sub>6</sub> octahedra is formed between Mo(1) and O(1), O(2), O(3),

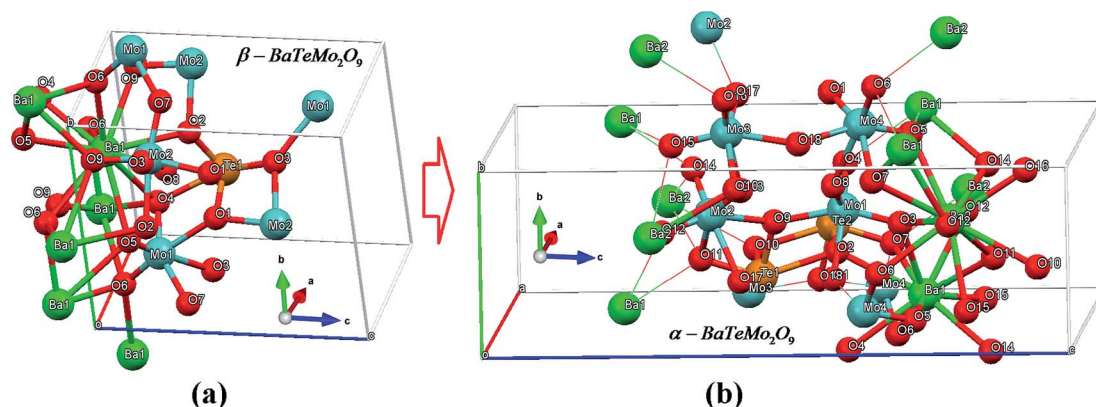


Fig. 1 (a) Molecule of  $\beta$ -BaTeMo<sub>2</sub>O<sub>9</sub> phase which show in  $\beta$ -BaTeMo<sub>2</sub>O<sub>9</sub> there is one TeO<sub>4</sub> polyhedra and the two MoO<sub>6</sub> octahedra; (b) molecule of  $\alpha$ -BaTeMo<sub>2</sub>O<sub>9</sub> phase which show in  $\alpha$ -BaTeMo<sub>2</sub>O<sub>9</sub> there are one TeO<sub>4</sub> polyhedra, one TeO<sub>3</sub> polyhedra and four MoO<sub>6</sub> octahedra.

O(4), O(8), O(9), the second Mo(2)O<sub>6</sub> octahedra is formed between Mo(2) and O(9), O(11), O(12), O(13), O(14), O(17), the third Mo(3)O<sub>6</sub> octahedra is formed between Mo(3) and O(10), O(13), O(15), O(16), O(17), O(18) and the fourth Mo(4)O<sub>6</sub> octahedra is formed between Mo(4) and O(1), O(5), O(6), O(7), O(8), O(18). The asymmetric unit of  $\alpha$ -BaTeMo<sub>2</sub>O<sub>9</sub> phase has a Ba<sub>2</sub>Te<sub>2</sub>Mo<sub>4</sub>O<sub>18</sub> formula thus double of  $\beta$ -BaTeMo<sub>2</sub>O<sub>9</sub> phase as shown in Fig. 1(b). Therefore,  $\alpha$ -BaTeMo<sub>2</sub>O<sub>9</sub> phase possesses more complicated structure than  $\beta$ -BaTeMo<sub>2</sub>O<sub>9</sub> phase.

## 4. Results and discussion

### 4.1. Salient features of the band structures

Based on our calculated band structure within mBJ we found that  $\beta$ -BaTeMo<sub>2</sub>O<sub>9</sub> and  $\alpha$ -BaTeMo<sub>2</sub>O<sub>9</sub> phases exhibit indirect band gap of about 2.93 eV ( $\beta$ ) and 3.12 eV ( $\alpha$ ) in good agreement with the measured values 2.95 eV ( $\beta$ ) and 3.12 eV ( $\alpha$ ) obtained from UV-vis diffuse reflectance spectroscopy.<sup>1</sup> It is interesting to highlight that previous calculations based on CASTEP code within LDA and GGA exhibit that the  $\beta$ -BaTeMo<sub>2</sub>O<sub>9</sub> possess a band gap of about 2.61 eV (LDA) and 2.67 eV (GGA).<sup>8</sup> While the ABINIT code within GGA show that  $\beta$ -BaTeMo<sub>2</sub>O<sub>9</sub> have a gap of about 2.78 eV.<sup>9</sup> Thus, it is clear that the mBJ approach succeeded by large amount in bringing the calculated energy gap closer to the experimental one as we expected from this approach.<sup>19,27</sup>

### 4.2. Linear optical properties and birefringence

In our previous work we have comprehensively investigated the band structure dispersion, density of states and the electronic charge density distribution of  $\beta$ -BaTeMo<sub>2</sub>O<sub>9</sub> and  $\alpha$ -BaTeMo<sub>2</sub>O<sub>9</sub> phases.<sup>28</sup> From the calculated properties we found that the two phases exhibit very promising structures. Thus, we are interested to explore and exploit the electronic structure of these two phases therefore, for deep insight into the electronic structure the optical properties of the two phases were investigated and analyzed in details. We have calculated the imaginary and real parts of the frequency dependent optical dielectric functions. The calculations of the frequency-dependent dielectric function involve the energy eigenvalues and electron wave functions. The optical components are determined by inter-band transitions from valence- into conduction-bands. According to the dipolar selection rule only transitions changing the angular momentum quantum number  $l$  by unity ( $\Delta = \pm 1$ ) are allowed.

The linear response of the system to electromagnetic radiation can be described by means of the dielectric function  $\epsilon(\omega) = \epsilon_1(\omega) + i\epsilon_2(\omega)$  which is related to the interaction of photons with electrons. Two kinds of contributions to  $\epsilon(\omega)$  are usually distinguished, namely intra-band (Drude term) and inter-band electronic excitations. Drude term is not present in semiconductors, it is present only for metals and semi-metals. The dispersion of the imaginary part of the dielectric function  $\epsilon_2^{xx}(\omega)$ ,  $\epsilon_2^{yy}(\omega)$  and  $\epsilon_2^{zz}(\omega)$  can be calculated from the momentum matrix elements between the occupied and unoccupied wave functions, giving rise to the selection rules as shown in Fig. 2(a) and (b). In order to identify the spectral structures in  $\epsilon_2^{xx}(\omega)$ ,  $\epsilon_2^{yy}(\omega)$  and  $\epsilon_2^{zz}(\omega)$  we need to look at the

magnitude of the optical matrix elements. The observed structures would correspond to those transitions that have large optical matrix elements. We have indicated these transitions in our calculated band structure and partial density of states diagrams (Fig. S as ESI†). The electronic band structure and the associated partial density of states suggests that the first spectral structure in  $\epsilon_2^{xx}(\omega)$ ,  $\epsilon_2^{yy}(\omega)$  and  $\epsilon_2^{zz}(\omega)$  is due to the transition from O-s/p, Te-s/p/d, Ba-s and Mo-s/p states to Te-s/p/d, O-s/p, Ba-s and Mo-s/p states. The second structure corresponds to transition between Mo-s/p/d, Ba-s, O-s/p, Te-s/p/d states and O-s/p, Te-s/p/d, Ba-s/d, Ta-s/p/d states. A remarkable fact regarding the first peak in  $\epsilon_2^{xx}(\omega)$ ,  $\epsilon_2^{yy}(\omega)$  and  $\epsilon_2^{zz}(\omega)$  is that its width is essentially determined by the width of the highest occupied valence band. Broadening is taken to be 0.1 eV which is traditional for oxide crystals and is typical of the experimental accuracy. Following Fig. 2(a) and (b) we notice that the fundamental optical absorption edge for  $\epsilon_2^{xx}(\omega)$ ,  $\epsilon_2^{yy}(\omega)$  and  $\epsilon_2^{zz}(\omega)$  are 2.92 and 3.12 eV for  $\beta$ -BaTeMo<sub>2</sub>O<sub>9</sub> and  $\alpha$ -BaTeMo<sub>2</sub>O<sub>9</sub> phases, respectively. The edges of the optical absorption give the threshold for direct optical transitions between the top of valence band and bottom of conduction band. We would like to mention that there exists a considerable anisotropy between the three principal complex tensor components  $\epsilon_2^{xx}(\omega)$ ,  $\epsilon_2^{yy}(\omega)$  and  $\epsilon_2^{zz}(\omega)$ , the anisotropy varies from  $\beta$ -phase to  $\alpha$ -phase. We should emphasize that the anisotropy in the linear optical susceptibilities favors an enhanced phase matching conditions necessary for observation of the second harmonic generation (SHG) and optical parametric oscillation (OPO).

The real part  $\epsilon_1^{xx}(\omega)$ ,  $\epsilon_1^{yy}(\omega)$  and  $\epsilon_1^{zz}(\omega)$  of the corresponding principal complex tensor components are obtained from the imaginary part of these principal complex tensor components by means of Kramers–Kronig transformation<sup>29</sup> as shown in Fig. 2(a) and (b). The vanishing frequency value of the dielectric function defines the static electronic dielectric constant  $\epsilon_1^{xx}(0)$ ,  $\epsilon_1^{yy}(0)$  and  $\epsilon_1^{zz}(0)$ . Table 1 shows the static electronic dielectric constant of  $\beta$ -BaTeMo<sub>2</sub>O<sub>9</sub> and  $\alpha$ -BaTeMo<sub>2</sub>O<sub>9</sub> phases. It has been found that  $\beta$ -BaTeMo<sub>2</sub>O<sub>9</sub> phase yields a larger  $\epsilon_1^{\text{average}}(0)$  value than that for  $\alpha$ -BaTeMo<sub>2</sub>O<sub>9</sub> phase. Therefore, a smaller energy gap yields a larger  $\epsilon_1^{\text{average}}(0)$  value. This could be explained on the basis of the Penn model.<sup>30</sup> Penn proposed a relation between  $\epsilon(0)$  and  $E_g$ ,  $\epsilon(0) \approx 1 + (\hbar\omega_p/E_g)^2$ .  $E_g$  is some kind of averaged energy gap which could be related to the real energy gap.

There are other important features in the optical spectrum, such as the uniaxial anisotropy  $\delta\epsilon = [(\epsilon_0^{\parallel} - \epsilon_0^{\perp})/\epsilon_0^{\text{average}}]$  which can be obtained from the static electronic dielectric constant  $\epsilon_1^{xx}(0)$ ,  $\epsilon_1^{yy}(0)$ ,  $\epsilon_1^{zz}(0)$  and  $\epsilon_1^{\text{average}}(0)$ . Since in  $\beta$ -BaTeMo<sub>2</sub>O<sub>9</sub> phase the value of  $\epsilon_1^{xx}(0)$  is closer to that of  $\epsilon_1^{zz}(0)$  therefore  $\frac{\epsilon_1^{xx}(0) + \epsilon_1^{zz}(0)}{2}$  represent  $\epsilon_1^{\perp}(\omega)$  while  $\epsilon_1^{yy}(0)$  represents  $\epsilon_1^{\parallel}(\omega)$ . Whereas in  $\alpha$ -BaTeMo<sub>2</sub>O<sub>9</sub> phase  $\frac{\epsilon_1^{yy}(0) + \epsilon_1^{zz}(0)}{2}$  represent  $\epsilon_1^{\perp}(\omega)$  and  $\epsilon_1^{xx}(0)$  represents  $\epsilon_1^{\parallel}(\omega)$ . It has been found that these materials exhibit positive uniaxial anisotropy and  $\alpha$ -phase shows higher value than  $\beta$ -phase, these values are listed in Table 1. The other features in the optical spectrum are the plasmon oscillations  $\omega_p^{xx}$ ,  $\omega_p^{yy}$  and  $\omega_p^{zz}$ , which are associated with inter-band transitions. The plasmon maximum is usually the most

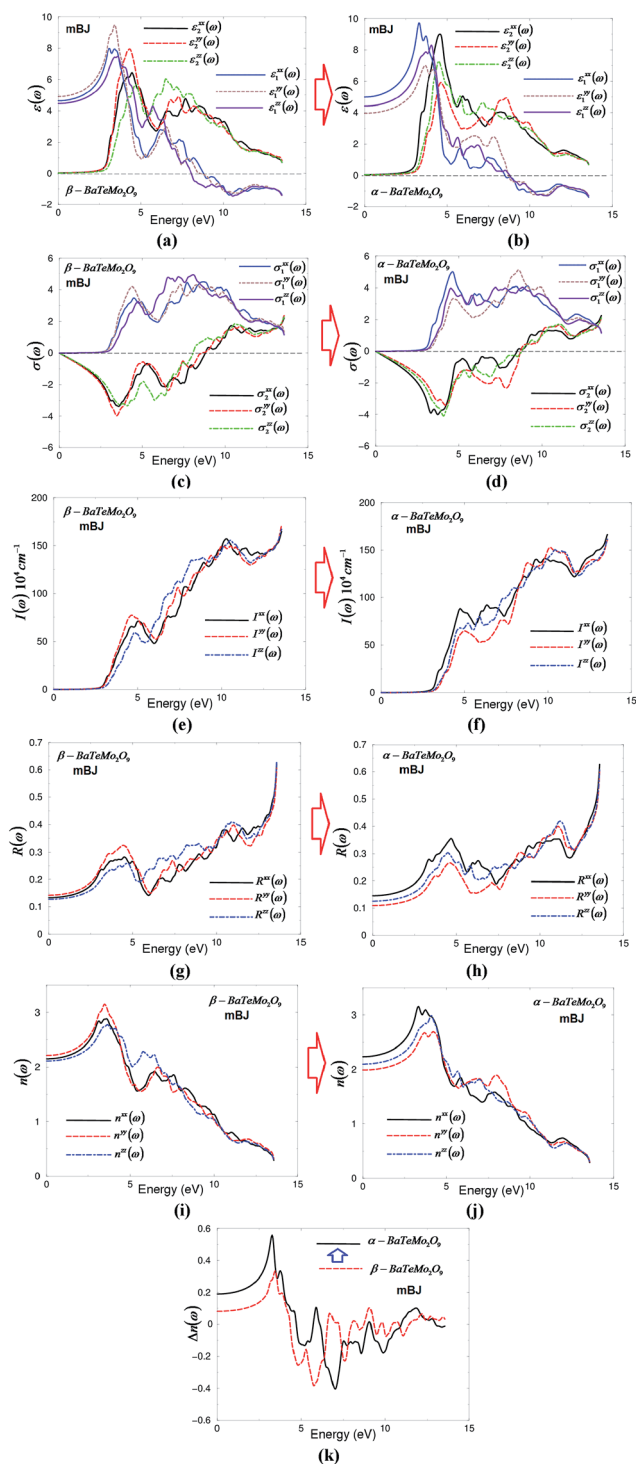


**Fig. 2** (a) Calculated  $\epsilon_2^{xx}(\omega)$  (dark solid curve-black color online),  $\epsilon_2^{yy}(\omega)$  (light long dashed curve-red color online) and  $\epsilon_2^{zz}(\omega)$  (light dotted dashed curve-green color online) along with calculated  $\epsilon_1^{xx}(\omega)$  (dark solid curve-blue color online),  $\epsilon_1^{yy}(\omega)$  (light dashed curve-brown color online) and  $\epsilon_1^{zz}(\omega)$  (light solid curve-violet color online) for  $\beta$ -BaTeMo<sub>2</sub>O<sub>9</sub>; (b) calculated  $\epsilon_2^{xx}(\omega)$  (dark solid curve-black color online),  $\epsilon_2^{yy}(\omega)$  (light long dashed curve-red color online) and  $\epsilon_2^{zz}(\omega)$  (light dotted dashed curve-green color online) along with calculated  $\epsilon_1^{xx}(\omega)$  (dark solid curve-blue color online),  $\epsilon_1^{yy}(\omega)$  (light dashed curve-brown color online) and  $\epsilon_1^{zz}(\omega)$  (light solid curve-violet color online) for  $\alpha$ -BaTeMo<sub>2</sub>O<sub>9</sub>; (c) calculated  $\sigma_2^{xx}(\omega)$  (dark solid curve-black color online),  $\sigma_2^{yy}(\omega)$  (light dashed curve-red color online) and  $\sigma_2^{zz}(\omega)$  (light dotted

intense feature in the spectrum and this is at energy where  $\epsilon_1^{xx}(\omega)$ ,  $\epsilon_1^{yy}(\omega)$  and  $\epsilon_1^{zz}(\omega)$  crosses zero which is associated with the existence of plasma oscillations. The obtained values of the plasma frequency are presented in Table 1. In order to gain more detailed information regarding the electronic structure of  $\beta$ -BaTeMo<sub>2</sub>O<sub>9</sub> and  $\alpha$ -BaTeMo<sub>2</sub>O<sub>9</sub> phases, the optical conductivity  $\sigma(\omega)$ , absorption coefficient  $I(\omega)$ , reflectivity spectra  $R(\omega)$ , refractive indices  $n(\omega)$  and the associated birefringence  $\Delta n(\omega)$  were calculated and compared with the available experimental data.<sup>1-3,10,11</sup>

The optical conductivity  $\sigma_2(\omega)$  and  $\sigma_1(\omega)$  were calculated using the expression  $\epsilon(\omega) = \epsilon_1(\omega) + i\epsilon_2(\omega) = 1 + \frac{4\pi i\sigma(\omega)}{\omega}$ , and presented in Fig. 2(c) and (d). The expression show that  $\sigma(\omega)$  is directly related to the complex dielectric function. The imaginary part  $\sigma_2^{xx}(\omega)$ ,  $\sigma_2^{yy}(\omega)$  and  $\sigma_2^{zz}(\omega)$  between 0.0 and the values of  $\omega_p^{xx}$ ,  $\omega_p^{yy}$  and  $\omega_p^{zz}$  exhibit overturned features of  $\epsilon_2^{xx}(\omega)$ ,  $\epsilon_2^{yy}(\omega)$  and  $\epsilon_2^{zz}(\omega)$ , whereas the real parts  $\sigma_1^{xx}(\omega)$ ,  $\sigma_1^{yy}(\omega)$  and  $\sigma_1^{zz}(\omega)$  show similar features to that of  $\epsilon_2^{xx}(\omega)$ ,  $\epsilon_2^{yy}(\omega)$  and  $\epsilon_2^{zz}(\omega)$ .

The calculated absorption coefficient  $I(\omega)$  of  $\beta$ -BaTeMo<sub>2</sub>O<sub>9</sub> and  $\alpha$ -BaTeMo<sub>2</sub>O<sub>9</sub> phases, presented in Fig. 2(e) and (f), shows the fundamental optical absorption edges situated at 2.85 and 3.11 eV thus matching the experimental value of the absorption edges (2.95 and 3.12 eV).<sup>1</sup> It has been noticed that  $I^{xx}(\omega)$ ,  $I^{yy}(\omega)$  and  $I^{zz}(\omega)$  of both phases increases drastically after the fundamental optical absorption edges. We should emphasize that  $\beta$ - and  $\alpha$ -phases exhibit a wide optical transparency region (886–4350 Å) and (886–3987 Å), respectively.

dashed curve-green color online) along with calculated  $\sigma_1^{xx}(\omega)$  (dark solid curve-blue color online),  $\sigma_1^{yy}(\omega)$  (light dashed curve-red brown online) and  $\sigma_1^{zz}(\omega)$  (light solid curve-violet color online) for  $\beta$ -BaTeMo<sub>2</sub>O<sub>9</sub>; (d) calculated  $\sigma_2^{xx}(\omega)$  (dark solid curve-black color online),  $\sigma_2^{yy}(\omega)$  (light dashed curve-red color online) and  $\sigma_2^{zz}(\omega)$  (light dotted dashed curve-green color online) along with calculated  $\sigma_1^{xx}(\omega)$  (dark solid curve-blue color online),  $\sigma_1^{yy}(\omega)$  (light dashed curve-red brown online) and  $\sigma_1^{zz}(\omega)$  (light solid curve-violet color online) for  $\alpha$ -BaTeMo<sub>2</sub>O<sub>9</sub>; (e) calculated absorption coefficient  $I^{xx}(\omega)$  (dark solid curve-back color online),  $I^{yy}(\omega)$  (light dashed curve-red color online) and  $I^{zz}(\omega)$  (light dotted dashed curve-blue color online) spectrum for  $\beta$ -BaTeMo<sub>2</sub>O<sub>9</sub>, the absorption coefficient in  $10^4 \text{ cm}^{-1}$ ; (f) calculated absorption coefficient  $I^{xx}(\omega)$  (dark solid curve-back color online),  $I^{yy}(\omega)$  (light dashed curve-red color online) and  $I^{zz}(\omega)$  (light dotted dashed curve-blue color online) spectrum for  $\alpha$ -BaTeMo<sub>2</sub>O<sub>9</sub>, the absorption coefficient in  $10^4 \text{ cm}^{-1}$ ; (g) calculated  $R^{xx}(\omega)$  (dark solid curve-black color online),  $R^{yy}(\omega)$  (light dashed curve-red color online), and  $R^{zz}(\omega)$  (light dotted dashed curve-blue color online) for  $\beta$ -BaTeMo<sub>2</sub>O<sub>9</sub>; (h) calculated  $R^{xx}(\omega)$  (dark solid curve-black color online),  $R^{yy}(\omega)$  (light dashed curve-red color online), and  $R^{zz}(\omega)$  (light dotted dashed curve-blue color online) for  $\alpha$ -BaTeMo<sub>2</sub>O<sub>9</sub>; (i) calculated refractive indices  $n^{xx}(\omega)$  (dark solid curve-black color online),  $n^{yy}(\omega)$  (light dashed curve-red color online) and  $n^{zz}(\omega)$  (light dotted dashed curve-blue color online) spectrum  $\beta$ -BaTeMo<sub>2</sub>O<sub>9</sub>; (j) calculated refractive indices  $n^{xx}(\omega)$  (dark solid curve-black color online),  $n^{yy}(\omega)$  (light dashed curve-red color online) and  $n^{zz}(\omega)$  (light dotted dashed curve-blue color online) spectrum  $\alpha$ -BaTeMo<sub>2</sub>O<sub>9</sub>; (k) calculated birefringence  $\Delta n(\omega)$  for  $\alpha$ -BaTeMo<sub>2</sub>O<sub>9</sub> (dark solid curve-black color online) and  $\beta$ -BaTeMo<sub>2</sub>O<sub>9</sub> (light long dashed curve-red color online).

The calculated optical reflectivity spectra  $R^{xx}(\omega)$ ,  $R^{yy}(\omega)$  and  $R^{zz}(\omega)$  along the polarization directions [100], [101] and [001] are shown in Fig. 2(g) and (h). It has been found that the first reflectivity minima occurs between 7.0 and 9.0 eV for  $\beta$ - and  $\alpha$ -phases, the region where the values of plasma resonance situated that confirms the occurrence of a collective plasmon resonance in concordance with our observation in Fig. 2(a–d).

Further, we have calculated the refractive indices of  $\beta$ - and  $\alpha$ -phases as shown in Fig. 2(i) and (j). The calculated values of the refractive indices at the static limit and at  $\lambda = 0.4 \mu\text{m}$  show reasonable agreement with the experimental data.<sup>3,13</sup> These values are listed in Table 1. It has been noticed that  $n^{xx}(\omega)$ ,  $n^{yy}(\omega)$  and  $n^{zz}(\omega)$  reach their maximum at the energy region between 3.0 and 3.5 eV, then gradually decreases to go beyond unity, they cross the unity at the values of  $\omega_p^{xx}$ ,  $\omega_p^{yy}$  and  $\omega_p^{zz}$ . From the calculated refractive indices we can plot the birefringence curve and obtain the birefringence values at static limit and at any wavelength. The birefringence is important only in the non-absorbing spectral range, which is below the energy gap. The birefringence is the difference between the extraordinary and ordinary refraction indices,  $\Delta n(\omega) = n_e(\omega) - n_o(\omega)$ , where  $n_o(\omega)$  is the index of refraction for an electric field oriented along the  $c$ -axis and  $n_e(\omega)$  is the index of refraction for an electric field perpendicular to the  $c$ -axis. Fig. 2(k) shows the birefringence  $\Delta n(\omega)$  dispersion of  $\beta$ - and  $\alpha$ -phases. The calculated birefringence at zero limit and at  $\lambda = 404.7 \text{ nm}$  in comparison with the experimental values<sup>3,13</sup> are listed in Table 1. It has been found the both phases exhibit a positive birefringence and  $\alpha$ -phase show higher birefringence's value than that of  $\beta$ -phase indicating that  $\alpha$ -phase exhibit higher anisotropy than that of  $\beta$ -phase in concordance with our observation from  $\delta\varepsilon$  values (Table 1).

### 4.3. Second harmonic generation and hyperpolarizability

$\beta$ -BaTeMo<sub>2</sub>O<sub>9</sub> and  $\alpha$ -BaTeMo<sub>2</sub>O<sub>9</sub> phases crystallized in non-centro-symmetry structure results in the loss of the inversion

symmetry which in turn gives a non-zero second harmonic generation (SHG). The monoclinic structure with space group  $P2_1$  allows eight nonzero complex second-order nonlinear optical susceptibility tensors  $\chi_{112}^{(2)}(-2\omega; \omega; \omega)$ ,  $\chi_{123}^{(2)}(-2\omega; \omega; \omega)$ ,  $\chi_{211}^{(2)}(-2\omega; \omega; \omega)$ ,  $\chi_{222}^{(2)}(-2\omega; \omega; \omega)$ ,  $\chi_{231}^{(2)}(-2\omega; \omega; \omega)$ ,  $\chi_{233}^{(2)}(-2\omega; \omega; \omega)$ ,  $\chi_{312}^{(2)}(-2\omega; \omega; \omega)$  and  $\chi_{323}^{(2)}(-2\omega; \omega; \omega)$ . Whereas the orthorhombic  $Pca2_1$  space group allows only five nonzero complex second-order nonlinear optical susceptibility tensors  $\chi_{113}^{(2)}(-2\omega; \omega; \omega)$ ,  $\chi_{223}^{(2)}(-2\omega; \omega; \omega)$ ,  $\chi_{311}^{(2)}(-2\omega; \omega; \omega)$ ,  $\chi_{322}^{(2)}(-2\omega; \omega; \omega)$  and  $\chi_{333}^{(2)}(-2\omega; \omega; \omega)$ . It is well known that the nonlinear optical properties are more sensitive to small changes in the band structure than the linear optical properties,<sup>31</sup> since the asymmetric unit of  $\beta$ -BaTeMo<sub>2</sub>O<sub>9</sub> phase has a BaTeMo<sub>2</sub>O<sub>9</sub> formula while the asymmetric unit of  $\alpha$ -BaTeMo<sub>2</sub>O<sub>9</sub> phase has a Ba<sub>2</sub>Te<sub>2</sub>Mo<sub>4</sub>O<sub>18</sub> formula, this will arise differences in the band structures and wave-functions. Therefore, we expected that the  $\alpha$ -phase will exhibit higher SHG than that of  $\beta$ -phase. But as we had mentioned before that in  $\alpha$ -BaTeMo<sub>2</sub>O<sub>9</sub>, there are one TeO<sub>4</sub> polyhedra, one TeO<sub>3</sub> polyhedra and four MoO<sub>6</sub> octahedra, which are responsible for the high local SHG response. However, the arrangement of the dipole moments in TeO<sub>4</sub>, TeO<sub>3</sub> and four MoO<sub>6</sub> are not oriented parallel to each others which cause to produce local SHG signals in random directions resulting in weaken the net SHG<sup>1</sup> in  $\alpha$ -BaTeMo<sub>2</sub>O<sub>9</sub> phase. While the arrangement of the dipole moments in TeO<sub>4</sub> polyhedra and the two MoO<sub>6</sub> octahedra of  $\beta$ -BaTeMo<sub>2</sub>O<sub>9</sub> phase in a way cause to strengthen the net SHG.<sup>1</sup> That is attributed to the fact that the SHG response in the non-centro-symmetric materials is due to the anionic group according to Chen's anionic group theory.<sup>32</sup>

The SHG is very sensitive to the energy gap's value as the energy gap comes in the denominator of the formulae (2)–(4).<sup>21–24</sup> Although mBJ approach succeed by large amount in bringing the calculated energy gap closer to the experimental one thus, we have applied the scissors correction to bring the value of the calculated energy gap exactly to the measured gap.

**Table 1** The calculated energy band gap in comparison with the experimental value,  $\varepsilon_1^{xx}(0)$ ,  $\varepsilon_1^{yy}(0)$ ,  $\varepsilon_1^{zz}(0)$ ,  $\varepsilon_1^{\text{average}}(0)$ ,  $\delta\varepsilon$ ,  $\omega_p^{xx}$ ,  $\omega_p^{yy}$ ,  $\omega_p^{zz}$ ,  $n^{xx}(0)$ ,  $n^{yy}(0)$ ,  $n^{zz}(0)$  and  $\Delta n(0)$

|                                     | $\beta$ -BaTeMo <sub>2</sub> O <sub>9</sub>    |   | $\alpha$ -BaTeMo <sub>2</sub> O <sub>9</sub>   |  |
|-------------------------------------|--|---|--|--|
|                                     | This work                                      | Exp.  | This work                                      | Exp.   |
| Eg (eV)                             | 2.93 (mBJ)*                                    | 2.95 <sup>a</sup>                                   | 3.12 (mBJ)*                                    | 3.12 <sup>a</sup>  |
| $\varepsilon_1^{xx}(0)$             | 4.63   |   | 4.99   |  |
| $\varepsilon_1^{yy}(0)$             | 4.91   |   | 4.00   |  |
| $\varepsilon_1^{zz}(0)$             | 4.46   |   | 4.40   |  |
| $\varepsilon_1^{\text{average}}(0)$ | 4.66   |   | 4.46   |  |
| $\delta\varepsilon$                 | 0.078  |   | 0.177  |  |
| $\omega_p^{xx}$                     | 8.82   |   | 8.47   |  |
| $\omega_p^{yy}$                     | 8.47   |   | 8.70   |  |
| $\omega_p^{zz}$                     | 8.05   |   | 8.79   |  |
| $n^{xx}(0)$                         | 2.15*, 2.84* ( $\lambda = 0.4 \mu\text{m}$ )   |   | 2.24*, 2.94* ( $\lambda = 0.4 \mu\text{m}$ )   | 2.12 <sup>b,c</sup> ( $\lambda = 0.4 \mu\text{m}$ )  |
| $n^{yy}(0)$                         | 2.21*, 2.97* ( $\lambda = 0.4 \mu\text{m}$ )   |   | 1.99*, 2.37* ( $\lambda = 0.4 \mu\text{m}$ )   | 2.16 <sup>b</sup> ( $\lambda = 0.4 \mu\text{m}$ )  |
| $n^{zz}(0)$                         | 2.11*, 2.59* ( $\lambda = 0.4 \mu\text{m}$ )   |   | 2.09, 2.57* ( $\lambda = 0.4 \mu\text{m}$ )    | 2.43 <sup>b</sup> ( $\lambda = 0.4 \mu\text{m}$ ), 2.42 <sup>c</sup> ( $\lambda = 0.4 \mu\text{m}$ ) |
| $\Delta n(0)$                       | 0.080, 0.210* ( $\lambda = 404.7 \text{ nm}$ ) | 0.198 <sup>b</sup> ( $\lambda = 404.7 \text{ nm}$ ) | 0.187, 0.440* ( $\lambda = 404.7 \text{ nm}$ ) | 0.305 <sup>b,c</sup> ( $\lambda = 404.7 \text{ nm}$ )  |

<sup>a</sup> Ref. 1. <sup>b</sup> Ref. 13. <sup>c</sup> Ref. 3.

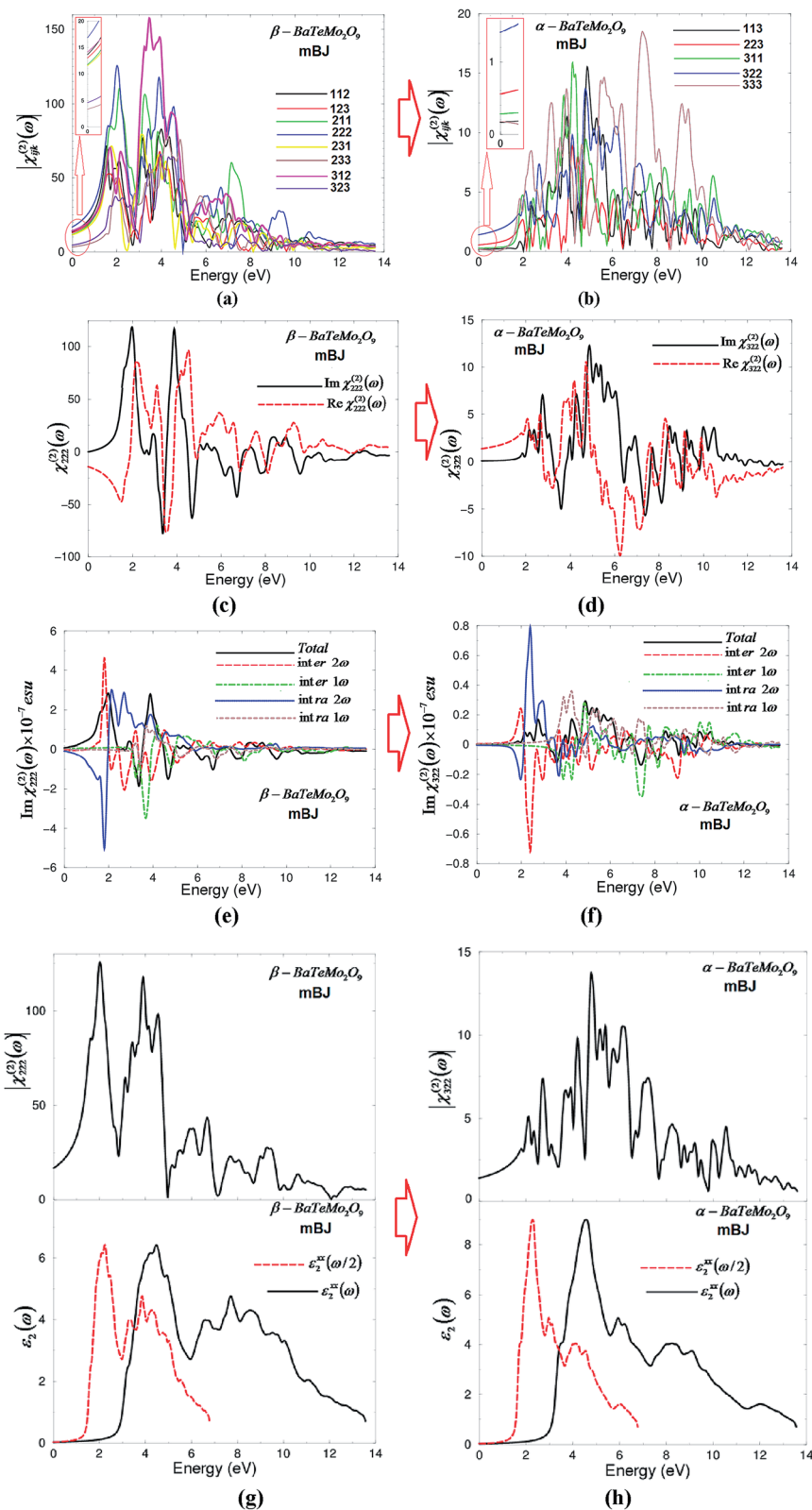


**Fig. 3** (a) Calculated  $|\chi_{ijk}^{(2)}(\omega)|$  for the eight tensor components of  $\beta$ -BaTeMo<sub>2</sub>O<sub>9</sub> phase; (b) calculated  $|\chi_{ijk}^{(2)}(\omega)|$  for the five tensor components of  $\alpha$ -BaTeMo<sub>2</sub>O<sub>9</sub> phase; (c) calculated imaginary  $\chi_{222}^{(2)}(\omega)$  (dark solid curve-black color online) and real  $\chi_{222}^{(2)}(\omega)$  (light dashed curve-red color online) spectra of  $\beta$ -BaTeMo<sub>2</sub>O<sub>9</sub> phase; (d) calculated imaginary  $\chi_{322}^{(2)}(\omega)$  (dark solid curve-black color online) and real  $\chi_{322}^{(2)}(\omega)$  (light dashed curve-red color online) spectra of  $\alpha$ -BaTeMo<sub>2</sub>O<sub>9</sub> phase; (e) calculated total  $\text{Im}\chi_{222}^{(2)}(\omega)$  spectrum (dark solid curve-black color online) along with the intra (2 $\omega$ )/(1 $\omega$ ) (light solid curve-blue color online)/(light dashed dotted curve-cyan color online) and inter (2 $\omega$ )/(1 $\omega$ ) (light long dashed curve-red color online)/(light dotted curve-green color online) -band contributions of  $\beta$ -BaTeMo<sub>2</sub>O<sub>9</sub> phase, here all  $\text{Im}\chi_{222}^{(2)}(\omega)$  are multiplied by  $10^{-7}$ , in esu units; (f) calculated total  $\text{Im}\chi_{322}^{(2)}(\omega)$  spectrum (dark solid curve-black color online) along with the intra (2 $\omega$ )/(1 $\omega$ ) (light solid curve-blue color online)/

**Table 2** Calculated  $|\chi_{ijk}^{(2)}(\omega)|$  and  $\beta_{ijk}$  of  $\beta$ -BaTeMo<sub>2</sub>O<sub>9</sub> and  $\alpha$ -BaTeMo<sub>2</sub>O<sub>9</sub> in pm V<sup>-1</sup> at static limit and at  $\lambda = 1064$  nm along with measured values. Where  $1 \text{ pm V}^{-1} = 2.387 \times 10^{-9} \text{ esu}$ . Following this table we can see that  $\beta$ -BaTeMo<sub>2</sub>O<sub>9</sub> exhibit larger SHG than that of  $\alpha$ -BaTeMo<sub>2</sub>O<sub>9</sub> which is very close to the experimental value of the well known KTiOPO<sub>4</sub> (KTP) single crystals which exhibits a SHG value of about 16.9,<sup>33</sup> 13.7,<sup>34</sup> 15.4  $\pm$  0.2,<sup>35</sup> 14.6  $\pm$  1.0,<sup>36</sup> 17.4  $\pm$  1.7,<sup>37</sup> 16.9  $\pm$  3.3,<sup>38</sup> 16.9  $\pm$  1.7,<sup>39</sup> 10.6  $\pm$  7.5,<sup>40</sup> 16.75 (ref. 41) and 16.65.<sup>41</sup>

| $\beta$ -BaTeMo <sub>2</sub> O <sub>9</sub> |                              |  |  | $\alpha$ -BaTeMo <sub>2</sub> O <sub>9</sub> |                              |  |  |  |                          |
|---|------------------------------|--|--|--|------------------------------|--|--|--|--------------------------|
| Tensor components                           | Theory $\chi_{ijk}^{(2)}(0)$ | Theory $d_{ijk} = 0.5\chi_{ijk}^{(2)}(\omega)$ | $\chi_{ijk}^{(2)}(\omega)$ at $\lambda = 1064$           | Tensor components                            | Theory $\chi_{ijk}^{(2)}(0)$ | Theory $d_{ijk} = 0.5\chi_{ijk}^{(2)}(\omega)$ | $\chi_{ijk}^{(2)}(\omega)$ at $\lambda = 1064$ |  |                          |
| $ \chi_{112}^{(2)}(\omega) $                | 13.62                        | $d_{16} = 6.81$                                | 34.59  | $d_{16} = 17.30$                             | $ \chi_{113}^{(2)}(\omega) $ | 0.16   | $d_{15} = 0.08$                                | 0.27   | $d_{15} = 0.14$          |
| $ \chi_{123}^{(2)}(\omega) $                | 13.12                        | $d_{14} = 6.56$                                | 28.82  | $d_{14} = 14.41$                             | $ \chi_{223}^{(2)}(\omega) $ | 0.54   | $d_{24} = 0.27$                                | 0.92   | $d_{24} = 0.46$          |
| $ \chi_{211}^{(2)}(\omega) $                | 11.92                        | $d_{21} = 5.96$                                | 30.11  | $d_{21} = 15.06$                             | $ \chi_{311}^{(2)}(\omega) $ | 0.28   | $d_{31} = 0.14$                                | 0.41   | $d_{31} = 0.21$          |
| $ \chi_{222}^{(2)}(\omega) $                | <b>16.87</b>                 | $d_{22} = \mathbf{8.44}$                       | <b>40.91</b>   | $d_{22} = \mathbf{20.46}$                    | $ \chi_{322}^{(2)}(\omega) $ | <b>1.41</b>                                    | $d_{32} = \mathbf{0.71}$                       | <b>2.10</b>  | $d_{32} = \mathbf{0.11}$ |
| $ \chi_{231}^{(2)}(\omega) $                | 11.57                        | $d_{25} = 5.79$                                | 25.41  | $d_{25} = 12.71$                             | $ \chi_{333}^{(2)}(\omega) $ | 0.19   | $d_{33} = 0.095$                               | 0.25   | $d_{33} = 0.13$          |
| $ \chi_{233}^{(2)}(\omega) $                | 3.45                         | $d_{23} = 1.73$                                | 7.76   | $d_{23} = 3.88$                              | $\beta_{322}$                | $2.291 \times 10^{-30}$                        |  | $3.376 \times 10^{-30}$ at $(\lambda = 1064 \text{ nm})$ |                          |
| $ \chi_{312}^{(2)}(\omega) $                | 14.25                        | $d_{36} = 7.13$                                | 29.71  | $d_{36} = 14.86$                             |                              |  |  |  |                          |
| $ \chi_{323}^{(2)}(\omega) $                | 3.31                         | $d_{34} = 1.66$                                | 10.93  | $d_{34} = 5.47$                              |                              |  |  |  |                          |
| $\beta_{222}$                               | $6.787 \times 10^{-30}$      |  | $6.787 \times 10^{-30}$ at $(\lambda = 1064 \text{ nm})$ |  |                              |  |  |  |                          |

The scissors correction is the difference between the calculated and measured energy gaps. It is a consequence of a fact that the DFT calculations usually underestimate the energy gaps with respect to the experimental gaps. A very simple way to overcome this drawback is to use the scissors correction, which merely brings the calculated energy gap close to the experimental gap. It has been found that the scissors corrections has a profound effect on the magnitude of the complex second-order nonlinear optical susceptibility tensors.

Fig. 3(a) and (b) illustrated the calculated  $|\chi_{ijk}^{(2)}(\omega)|$  for the non-zero complex second-order nonlinear optical susceptibility tensors of  $\beta$ -BaTeMo<sub>2</sub>O<sub>9</sub> and  $\alpha$ -BaTeMo<sub>2</sub>O<sub>9</sub> phases.

It is clear that  $\beta$ -phase show  $|\chi_{222}^{(2)}(\omega)|$  as the dominant component among the others while  $|\chi_{322}^{(2)}(\omega)|$  is the dominant component in  $\alpha$ -phase. The calculated values of  $|\chi_{ijk}^{(2)}(\omega)|$  for both phases at static limit and at 1.165 eV ( $\lambda = 1064$  nm) were presented in Table 2 along with the other components. The static values of the second order susceptibility tensor are very important and can be used to estimate their relative SHG efficiency. Following this table we can see that  $\beta$ -BaTeMo<sub>2</sub>O<sub>9</sub> exhibit larger SHG than that of  $\alpha$ -BaTeMo<sub>2</sub>O<sub>9</sub>, which is very close to the experimental value of the well known KTiOPO<sub>4</sub> (KTP) single crystals which exhibits a SHG value of about 16.9,<sup>33</sup> 13.7,<sup>34</sup> 15.4  $\pm$  0.2,<sup>35</sup> 14.6  $\pm$  1.0,<sup>36</sup> 17.4  $\pm$  1.7,<sup>37</sup> 16.9  $\pm$  3.3,<sup>38</sup> 16.9  $\pm$  1.7,<sup>39</sup> 10.6  $\pm$  7.5,<sup>40</sup> 16.75 (ref. 41) and 16.65.<sup>41</sup>

The imaginary and real parts of the dominant component were calculated for  $\beta$ -BaTeMo<sub>2</sub>O<sub>9</sub> and  $\alpha$ -BaTeMo<sub>2</sub>O<sub>9</sub> phases as shown in Fig. 3(c) and (d). From the imaginary part we can see that both of  $\text{Im}\chi_{222}^{(2)}(\omega)$  and  $\text{Im}\chi_{322}^{(2)}(\omega)$  have zero value below half the band gap and slowly increases up after half the band gap since the  $2\omega$

resonance begin to contribute at energies above half the band gap due to  $E - 2\omega$  terms in the denominator of the formalism (2)–(4). The  $\omega$  resonance begins to contribute for energy values above the energy gap. At low spectral range (below half the energy band gap) the SHG optical spectra is dominated by the  $2\omega$  contributions. Beyond the fundamental energy gap (*i.e.*  $> 2.95$  eV ( $\beta$ ) and 3.12 eV ( $\alpha$ )) the major contribution comes from the  $\omega$  term. To support this statement we have plotted the  $2\omega/\omega$  inter-/intra-band contributions to the total  $\text{Im}\chi_{222}^{(2)}(\omega)$  and  $\text{Im}\chi_{322}^{(2)}(\omega)$  of the dominant components of  $\beta$ - and  $\alpha$ -phases. It is clear that each of  $\omega$  and  $2\omega$  resonances can be further separated into inter-band and intra-band contributions as shown in Fig. 3(e) and (f).

In order to understand the origin of the nonzero complex second-order nonlinear optical susceptibility tensors of  $\beta$ -BaTeMo<sub>2</sub>O<sub>9</sub> and  $\alpha$ -BaTeMo<sub>2</sub>O<sub>9</sub> phases therefore, we have analyzed the spectrum of the calculated dominant components  $|\chi_{222}^{(2)}(\omega)|$  and  $|\chi_{322}^{(2)}(\omega)|$  by correlated the features of this spectrum with the features of the absorptive part of the corresponding dielectric function  $\varepsilon_2(\omega)$  spectra in terms of single photon ( $\omega$ ) and two photon ( $\omega/2$ ) resonances as shown in Fig. 3(g) and (h). The spectral structure confined between 1.47–2.95 eV for  $\beta$ -BaTeMo<sub>2</sub>O<sub>9</sub> and 1.56–3.12 eV for  $\alpha$ -BaTeMo<sub>2</sub>O<sub>9</sub> is mainly originated from  $2\omega$  resonance. The next spectral structure between 2.95–7.0 eV ( $\beta$ -) and 3.12–7.0 eV ( $\alpha$ -) is associated with interference between  $2\omega$  and  $\omega$  resonances. The last spectral structure which is extended between 7.0–14.0 eV for both phases is mainly due to  $\omega$  resonance and is associated with the second structure in  $\varepsilon_2(\omega)$ .

We have calculated the microscopic first hyperpolarizability,  $\beta_{ijk}$ , the vector components along the dipole moment direction

(light dashed dotted curve-cyan color online) and inter ( $2\omega$ )/( $1\omega$ ) (light long dashed curve-red color online)/(light dotted curve-green color online) -band contributions of  $\alpha$ -BaTeMo<sub>2</sub>O<sub>9</sub> phase, here all  $\text{Im}\chi_{322}^{(2)}(\omega)$  are multiplied by  $10^{-7}$ , in esu units; (g) – upper panel – calculated  $|\chi_{222}^{(2)}(\omega)|$  (dark solid curve-black color online); – lower panel – calculated  $\varepsilon_2^{xx}(\omega)$  (dark solid curve-black color online); calculated  $\varepsilon_2^{xx}(\omega/2)$  (dark dashed curve-red color online) of  $\beta$ -BaTeMo<sub>2</sub>O<sub>9</sub> phase; (h) – upper panel – calculated  $|\chi_{322}^{(2)}(\omega)|$  (dark solid curve-black color online); – lower panel – calculated  $\varepsilon_2^{xx}(\omega)$  (dark solid curve-black color online); calculated  $\varepsilon_2^{xx}(\omega/2)$  (dark dashed curve-red color online) of  $\beta$ -BaTeMo<sub>2</sub>O<sub>9</sub> phase.

for the dominant components  $|\chi_{222}^{(2)}(\omega)|$  and  $|\chi_{322}^{(2)}(\omega)|$  of  $\beta$ -BaTeMo<sub>2</sub>O<sub>9</sub> and  $\alpha$ -BaTeMo<sub>2</sub>O<sub>9</sub> phases at static limit and at  $\lambda = 1064$  nm (1.165 eV), using  $\beta_{ijk}$  expression which is given elsewhere.<sup>42</sup> We should emphasize that the microscopic first hyperpolarizability terms cumulatively yield a bulk observable second order susceptibility term,  $\chi_{ijk}^{(2)}(\omega)$ , which in turn is responsible for the high SHG response.<sup>43,44</sup> These values are listed in Table 2.

We would like to mention here that in our previous works<sup>45,46</sup> we have calculated the linear and nonlinear optical susceptibilities using FPLAPW method on several systems whose linear and nonlinear optical susceptibilities are known experimentally, in those previous calculations we found very good agreement with the experimental data. Thus, we believe that our calculations reported in this paper would produce very accurate and reliable results.

## 5. Conclusions

In summary, we have performed calculations of the linear and nonlinear optical susceptibilities of  $\beta$ -BaTeMo<sub>2</sub>O<sub>9</sub> and  $\alpha$ -BaTeMo<sub>2</sub>O<sub>9</sub> phases. The underestimation of the energy gap is largely corrected by mBJ and partially by applying the scissors correction therefore, we obtained a results based on corrected gap which mach the experimental value. The calculated linear optical properties reveals that  $\alpha$ -BaTeMo<sub>2</sub>O<sub>9</sub> phases posses lower SHG than that of  $\beta$ -BaTeMo<sub>2</sub>O<sub>9</sub> phase due to orientation of the dipole moments in side TeO<sub>4</sub>, TeO<sub>3</sub> and four MoO<sub>6</sub> which cause to produce local SHG signals in random directions resulting in weaken the net SHG in  $\alpha$ -BaTeMo<sub>2</sub>O<sub>9</sub> phases.  $\beta$ -phase exhibit SHG close to the experimental value of the well known KTiOPO<sub>4</sub> (KTP) single crystals. We have analyzed the spectrum of the calculated dominant components by correlated the features of this spectrum with the features of  $\epsilon_2(\omega)$  spectra in terms of single photon ( $\omega$ ) and two photon ( $\omega/2$ ) resonances. We have calculated the microscopic first hyperpolarizability,  $\beta_{ijk}$ , the vector components along the dipole moment direction for the dominant components of  $\beta$ -BaTeMo<sub>2</sub>O<sub>9</sub> and  $\alpha$ -BaTeMo<sub>2</sub>O<sub>9</sub> phases at static limit and at  $\lambda = 1064$  nm.

## Acknowledgements

The result was developed within the CENTEM project, reg. no. CZ.1.05/2.1.00/03.0088, cofunded by the ERDF as part of the Ministry of Education, Youth and Sports OP RDI programme and, in the follow-up sustainability stage, supported through CENTEM PLUS (LO1402) by financial means from the Ministry of Education, Youth and Sports under the National Sustainability Programme I. Computational resources were provided by MetaCentrum (LM2010005) and CERIT-SC (CZ.1.05/3.2.00/08.0144) infrastructures.

## References

1 J. Zhang, Z. Zhang, W. Zhang, Q. Zheng, Y. Sun, C. Zhang and X. Tao, *Chem. Mater.*, 2011, **23**, 3752–3761.

- 2 A. Majchrowski, B. Sahraoui, A. O. Fedorchuk, L. R. Jaroszewicz, E. Michalski, A. Migalska-Zalas and I. V. Kityk, *J. Mater. Sci.*, 2013, **48**, 5938–5945.
- 3 Z. L. Gao, Q. Wu, X. T. Liu, Y. X. Sun and X. T. Tao, *Opt. Express*, 2015, **23**, 3851.
- 4 A. H. Reshak, H. Kamarudin, S. Auluck and I. V. Kityk, *J. Phys. Chem. B*, 2011, **115**, 11763–11769; A. H. Reshak, H. Kamarudin and S. Auluck, *J. Alloys Compd.*, 2011, **509**, 9685–9691.
- 5 I. Fuks-Janczarek, J. Luc, B. Sahraoui, F. Dumur, P. Hudhomme, J. Berdowski and I. V. Kityk, *J. Phys. Chem. B*, 2005, **109**(20), 10179–10183.
- 6 I. Fuks-Janczarek, S. Dabos-Seignon, B. Sahraoui, I. V. Kityk, J. Berdowski, E. Allard and J. Cousseau, *Opt. Commun.*, 2002, **211**(1–6), 303–308.
- 7 (a) A. Authier, *International Tables for Crystallography. Physical Properties of Crystals*, Kluwer Academic Publishers, Dordrecht, The Netherlands, 2003, vol. D; (b) J. F. Nye, *Physical Properties of Crystals: Their Representation by Tensors and Matrices*, Oxford University Press, New York, 1985; (c) S. R. Marder, G. D. Stucky and J. E. Sohn, *Materials for Nonlinear Optics: Chemical Perspectives*, *ACS Symposium Series 455*, American Chemical Society, Washington, DC, 1991; (d) R. Waser, U. B€ottger and S. Tiedke, *Polar Oxides: Properties, Characterization, and Imaging*, Wiley-VCH Verlag GmbH & Co. KGaA, Weinheim, 2005.
- 8 I. Fuks-Janczarek, R. Miedzinski, M. G. Brik, A. Majchrowski, L. R. Jaroszewicz and I. V. Kityk, *Solid State Sci.*, 2014, **27**, 30–35.
- 9 J. Zhang, X. F. Li, B. Xu and K. L. Yao, *J. Alloys Compd.*, 2011, **509**, 4929–4934.
- 10 (a) W. Zhang, X. Tao, C. Zhang, H. Zhang and M. Jiang, *Cryst. Growth Des.*, 2009, **9**, 2633–2636; (b) W. G. Zhang, X. T. Tao, C. Q. Zhang, Z. L. Gao, Y. Z. Zhang, W. T. Yu, X. F. Cheng, X. S. Liu and M. H. Jiang, *Cryst. Growth Des.*, 2008, **8**, 304–307.
- 11 W. Zhang, F. Li, S.-H. Kim and P. S. Halasyamani, *Cryst. Growth Des.*, 2010, **10**, 4091–4095.
- 12 J. Zhang, X. Tao, Y. Sun, Z. Zhang, C. Zhang, Z. Gao, H. Xia and S. Xia, *Cryst. Growth Des.*, 2011, **11**, 1863–1868.
- 13 J. Zhang, Z. Zhang, Y. Sun, C. Zhang and X. Tao, *CrystEngComm*, 2011, **13**, 6985.
- 14 S.-D. Liu, Ze-L. Gao, J.-J. Zhang, B.-T. Zhang, J.-L. He and Xu-T. Tao, *IEEE Photonics Technol. Lett.*, 2014, **26**, 15.
- 15 A. H. Reshak and S. Auluck, *RSC Adv.*, 2014, **4**, 37411.
- 16 M. Jamal, N. K. Sarvestani, A. Yazdani and A. H. Reshak, *RSC Adv.*, 2014, **4**, 57903.
- 17 P. Blaha, K. Schwarz, G. K. H. Madsen, D. Kvasnicka and J. Luitz, WIEN2k, *An augmented plane wave plus local orbitals program for calculating crystal properties*, Vienna University of Technology, Austria, 2001.
- 18 J. P. Perdew, S. Burke and M. Ernzerhof, *Phys. Rev. Lett.*, 1996, **77**, 3865.
- 19 F. Tran and P. Blaha, *Phys. Rev. Lett.*, 2009, **102**, 226401.
- 20 F. Bassani and G. P. Parravicini, “*Electronic States and Optical Transitions In Solids*” Pergamon Press Ltd., Oxford, 1975, pp. 149–154.

- 21 S. Sharma, J. K. Dewhurst and C. Ambrosch-Draxl, *Phys. Rev. B: Condens. Matter Mater. Phys.*, 2003, **67**, 165332.
- 22 S. N. Rashkeev, W. R. L. Lambrecht and B. Segall, *Phys. Rev. B: Condens. Matter Mater. Phys.*, 1998, **57**, 3905.
- 23 J. L. P. Hughes and J. E. Sipe, *Phys. Rev. B: Condens. Matter Mater. Phys.*, 1996, **53**, 10751.
- 24 V. I. Gavrilenko, *Phys. Status Solidi A*, 2001, **188**(4), 1267–1280.
- 25 C. Ambrosch-Draxl and J. Sofo, *Comput. Phys. Commun.*, 2006, **175**, 1–14.
- 26 D. E. Aspnes, *Phys. Rev. B: Solid State*, 1972, **6**, 4648.
- 27 A. H. Reshak, *RSC Adv.*, 2015, **5**, 22044.
- 28 A. H. Reshak, Article under consideration.
- 29 H. Tributsch, *Z. Naturforsch., A: Phys. Sci.*, 1977, **32**, 972.
- 30 D. R. Penn, *Phys. Rev. B: Solid State*, 1962, **128**, 2093.
- 31 A. H. Reshak, S. Auluck, D. Stys, I. V. Kityk, H. Kamarudin, J. Berdowski and Z. Tylczynski, *J. Mater. Chem.*, 2011, **21**, 17219.
- 32 (a) N. Ye, Q. Chen, B. Wu and C. Chen, *J. Appl. Phys.*, 1998, **84**, 555–558; (b) B. Wu, D. Tang, N. Ye and C. Chen, *Opt. Mater.*, 1996, **5**, 105–109; (c) C. Chuangtian, W. Yebin, W. Baichang, W. Keche, Z. Wenlun and Y. Linhua, *Nature*, 1995, **373**, 322–324.
- 33 K. Zhang and X. Wang, *Chin. Sci. Bull.*, 2001, **46**, 2028–2036.
- 34 <http://www.castech-us.com/casktp.htm>.
- 35 M. V. Pack, D. J. Armstrong and A. V. Smith, *Appl. Opt.*, 2004, **43**, 3319.
- 36 I. Shoji, T. Kondo, A. Kitamoto, M. Shirane and R. Ito, *J. Opt. Soc. Am. B*, 1997, **14**, 2268.
- 37 A. Anema and T. Rasing, *Appl. Opt.*, 1997, **36**, 5902.
- 38 L. K. Cheng, L. T. Cheng, J. Galperin, P. A. M. Hotsenpiller and J. D. Bierlein, *J. Cryst. Growth*, 1994, **137**, 107.
- 39 H. Vanherzeele and J. D. Bierlein, *Opt. Lett.*, 1992, **17**, 982.
- 40 B. Boulanger, J. P. Feve, G. Marnier and B. Menaert, *Pure Appl. Opt.*, 1998, **7**, 239.
- 41 A. H. Reshak, I. V. Kityk and S. Auluck, *J. Phys. Chem. B*, 2010, **114**, 16705–16712.
- 42 H. Vanherzeele and J. D. Bierlein, *Opt. Lett.*, 1992, **17**, 982.
- 43 R. Y. Boyd, *Principles of Nonlinear Optics*, NY, Academic Press, 1982, p. 420.
- 44 R. W. Boyd, *Nonlinear optics*, Academic Press is an imprint of Elsevier, 3rd edn, 2008, ISBN: 978-0-12-369470-6.
- 45 A. H. Reshak, V. Kityk and S. Auluck, *J. Phys. Chem. B*, 2010, **114**, 16705–16712.
- 46 A. H. Reshak, S. Auluck and I. V. Kityk, *J. Solid State Chem.*, 2008, **181**, 789–795.